PHYSICAL REVIEW A **95**, 061403(R) (2017)

Imaging the breakdown of molecular-frame dynamics through rotational uncoupling

Lucas J. Zipp,[1,2,*] Adi Natan,[1] and Philip H. Bucksbaum[1,2,3]
[1]*Stanford PULSE Institute, SLAC National Accelerator Laboratory, Menlo Park, California 94025, USA*
[2]*Department of Physics, Stanford University, Stanford, California 94305, USA*
[3]*Department of Applied Physics, Stanford University, Stanford, California 94305, USA*
(Received 19 July 2016; published 22 June 2017)

We demonstrate the breakdown of molecular-frame dynamics induced by the uncoupling of molecular rotation from electronic motion in molecular Rydberg states. We observe this non-Born-Oppenheimer regime in the time domain through photoelectron imaging of a coherent molecular Rydberg wave packet in N_2. The photoelectron angular distribution shows a radically different time evolution than that of a typical molecular-frame-fixed electron orbital, revealing the uncoupled motion of the electron as it precesses around the *averaged* anisotropic potential of the rotating ion core.

DOI: 10.1103/PhysRevA.95.061403

In the standard Born-Oppenheimer picture, electrons occupy orbitals that are fixed to the molecular frame and display the symmetries of the underlying molecular structure. Recent experiments in ultrafast and strong-field physics have utilized aligned ensembles of molecules, allowing for molecular-frame measurements of excited-state dynamics [1–4] and XUV and tunnel ionization [5–10] that are sensitive to electron orbital geometry. This simple picture breaks down for nonpenetrating Rydberg electrons, where the electron wave function has minimal overlap with the ion core. Coriolis-type forces can decouple the electron motion from the rotating core leading to a breakdown of Born-Oppenheimer molecular-frame dynamics in a process known as l-uncoupling [11].

The complex interplay between electronic and nuclear motion in the l-uncoupling regime presents a unique opportunity to study non-Born-Oppenheimer rotational-electronic coupling in molecules. The phenomenon of l-uncoupling has been previously inferred by the perturbed spacing of rotational levels of high-lying Rydberg states [12–17], but the dynamics have never before been observed directly.

Here we report the direct imaging in the time domain of the uncoupled motion of a molecular Rydberg electron. This is achieved through multiphoton preparation and subsequent photoelectron imaging of a coherent superposition of electronic states in the $4f$ Rydberg manifold of N_2. We track the angular motion of the l-uncoupled Rydberg electron and measure the effect of uncoupling on its laboratory-frame dynamics, providing a close view of the coherent dynamics of a molecular system in a non-Born-Oppenheimer regime. This work complements previous angle-integrated measurements of Rydberg molecules that have focused on other aspects of rotational-electronic coupling, most notably stroboscopic effects on the radial motion of a Rydberg wave packet [18–21].

The nl Rydberg manifold of a molecule consists of $(2l+1)$ states, which in the Born-Oppenheimer limit correspond to the quantized projections Λ of the electronic orbital angular momentum onto the internuclear axis. The coupling between the various angular momenta of a diatomic molecule can be characterized with basis sets known as Hund's cases [22]. In the case of the singlet Rydberg states of N_2, with electronic spin $S=0$, the transition to the l-uncoupling regime is then described as a change in basis from Hund's case (b) (the Born-Oppenheimer limit) to Hund's case (d) (the uncoupled limit). Excluding nuclear spin degrees of freedom, this corresponds to a change in quantum labels from $|JM;l\Lambda\rangle \rightarrow |JM;lR\rangle$, where J is the total angular momentum of the system with laboratory-frame projection M, l is the orbital angular momentum of the Rydberg electron, and R is the total angular momentum of the ion core. In the fully uncoupled limit, where the eigenstates of the system are given by Hund's case (d) states, the electron wave function is totally decoupled from the ion-core molecular frame. The full rotational-electronic Hamiltonian of a diatomic molecule is given by [23]

$$H = \hat{H}_{ev} + B\hat{R}^2, \tag{1}$$

where $\hat{H}_{ev}$ is the vibronic Born-Oppenheimer Hamiltonian and $\hat{R}$ corresponds to the rotational angular momentum of the nuclei with rotational constant B. $\hat{H}_{ev}$ is diagonal in the Born-Oppenheimer Hund's case (b) basis set, and for nonpenetrating Rydberg states, this energy is approximately

$$\langle \hat{H}_{ev}\rangle_{nl\Lambda} = E_{nl} + a\Lambda^2, \tag{2}$$

where E_{nl} is the nonrotating energy (electronic and vibrational) of the $|nl\,\Lambda=0\rangle$ Rydberg state and a is a constant that depends on the strength of the anisotropic interaction of the Rydberg electron with the core [16]. Nonpenetrating Rydberg states refers to Rydberg electrons with minimal overlap with the ion-core wave function, as is generally true for Rydberg electrons with $l>2$ [24]. When the electronic splitting is large relative to the rotational energy spacing of the system, which occurs when $a\Lambda^2 \gg BR^2$, then the Born-Oppenheimer approximation holds, and the electron wave function is firmly fixed to the molecular frame. As the electronic energy splitting between Λ states decreases relative to the rotational energy, the electronic motion and the nuclear rotation begin to mutually perturb each other. This results in the well-known behavior of Λ doubling, which removes the degeneracy between even and odd parity states for $\Lambda \neq 0$ [11]. If the electronic splitting is reduced further, the l-uncoupling regime is reached and the electron orbital angular momentum uncouples from the molecular axis and Λ is no longer a good

*lzipp@stanford.edu

quantum number. Instead, the eigenstates are characterized by the projection of the Rydberg electron orbital angular momentum onto the *rotational* axis of the core. The direct consequence is that by exciting a coherent superposition of sublevels in an l-uncoupled Rydberg manifold, the electron wave packet oscillates in the *time-average* molecular potential created by the rotating molecule. The frequency of these angular oscillations depends on the strength of the interaction of the Rydberg electron with the anisotropic ion-core potential and is independent of the rotational period of the core.

The transition from the Born-Oppenheimer regime to the l-uncoupled regime is accompanied by dramatic changes in the coupled electronic-nuclear angular dynamics. This can be visualized in the case of quasi-classical nuclear rotational wave packets, similar to those achievable with the optical centrifuge technique [25]. Using the Hamiltonian in Eq. (2), we simulate the electron and ion-core position density as a function of time (see Supplemental Material for details [26]). The Rydberg electron is initially aligned along the internuclear axis of the rotating molecule, and the ensuing dynamics of the system for several values of the electronic splitting parameter a are shown in Fig. 1. For large electronic splittings, the system follows Born-Oppenheimer dynamics, and the electronic wave function is tightly bound to the rotating internuclear axis (top row). As the interaction strength decreases between the Rydberg electron and the anisotropic part of the core potential, the electron motion first lags behind the core rotation before jumping ahead, producing an oscillatory motion resembling loosely coupled pendula (middle row). A further decrease in the anisotropic interaction strength leads to uncoupled motion of the electron and the core (bottom row). The nuclei continue to rotate, while the Rydberg electron density remains fixed in the laboratory reference frame, unperturbed by the nuclear motion.

The uncoupling behavior of Rydberg states can be observed directly in time- and angle-resolved photoelectron spectra. A multiphoton pump pulse initiates the l-uncoupling dynamics by exciting a molecular Rydberg manifold coupled to a coherent rotational wave packet. The state of the system may then be probed at later times through single-photon ionization of the Rydberg state. Through numerical simulations we can explore how the time-dependent photoelectron angular distribution (PAD) in this pump-probe scheme is expected to change with the transition from Born-Oppenheimer dynamics to the l-uncoupled regime. The simulations use the same Hamiltonian of Eq. (2) used to generate the visualization in Fig. 1, however, we now prepare the Rydberg wave packet assuming an impulsive, perturbative five-photon transition from the ground state to a $4f$ Rydberg manifold, and include an impulsive single-photon ionization step to create the photoelectron angular distribution. The PAD is then characterized by a sum of even-order Legendre polynomials,

$$I(\theta) = \frac{\sigma}{4\pi}[1 + \beta_2 P_2(\cos\theta) + \beta_4 P_4(\cos\theta) + \cdots], \qquad (3)$$

where σ is the total angle-integrated yield.

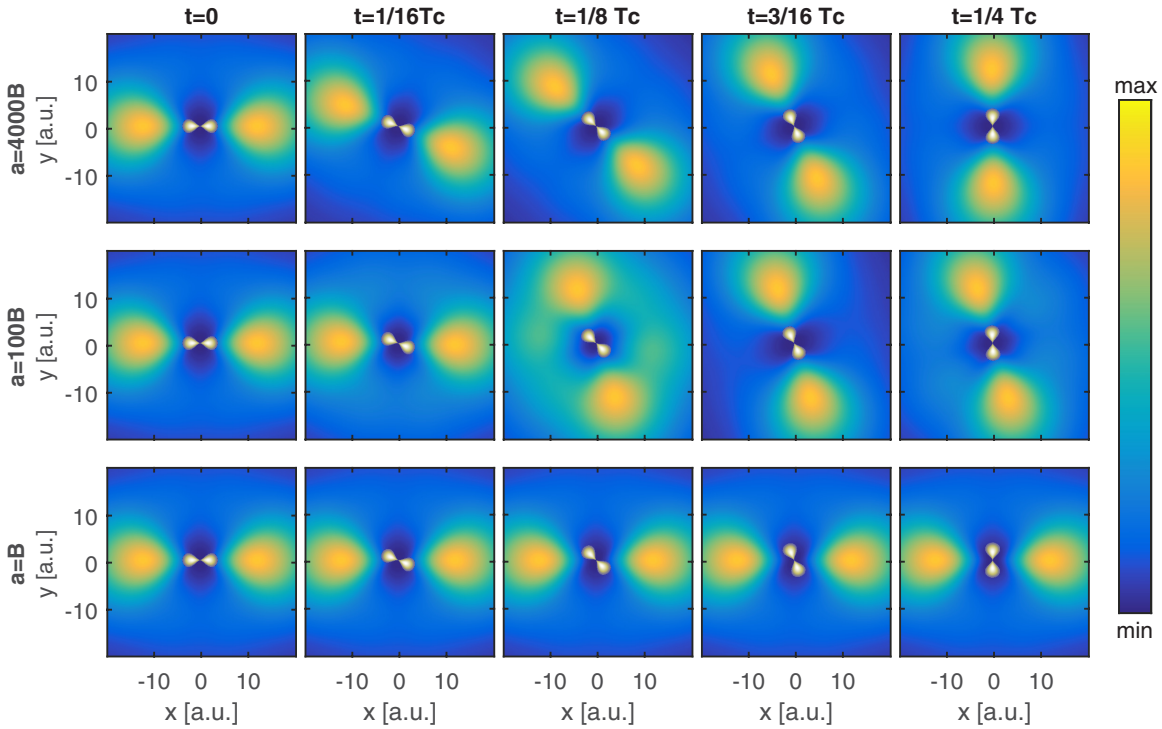

FIG. 1. Breakdown of molecular-frame dynamics. The outer lobes (blue-yellow color scale) correspond to the Rydberg electron density with a $4f$ orbital radial distribution, while the inner lobe (white) shows the angular distribution of the nuclei, with an artificially chosen radial distribution for better visualization. The simulated homonuclear diatomic system starts out in a localized rotational wave packet centered at $|J = 30, M = 30\rangle$ with an f Rydberg electron aligned along the internuclear axis in a $\Lambda = 0$ state. The electron and ion-core position densities are plotted at times corresponding to fractions of the classical nuclear rotation period, $T_c = \pi/[B\sqrt{J(J+1)}]$. Each row displays the dynamics for a different value of the electronic splitting parameter a, as given in Eq. (2). The top row corresponds to the Born-Oppenheimer regime, while the bottom row shows completely uncoupled nuclear and rotational dynamics (see Supplemental Material for full movies).

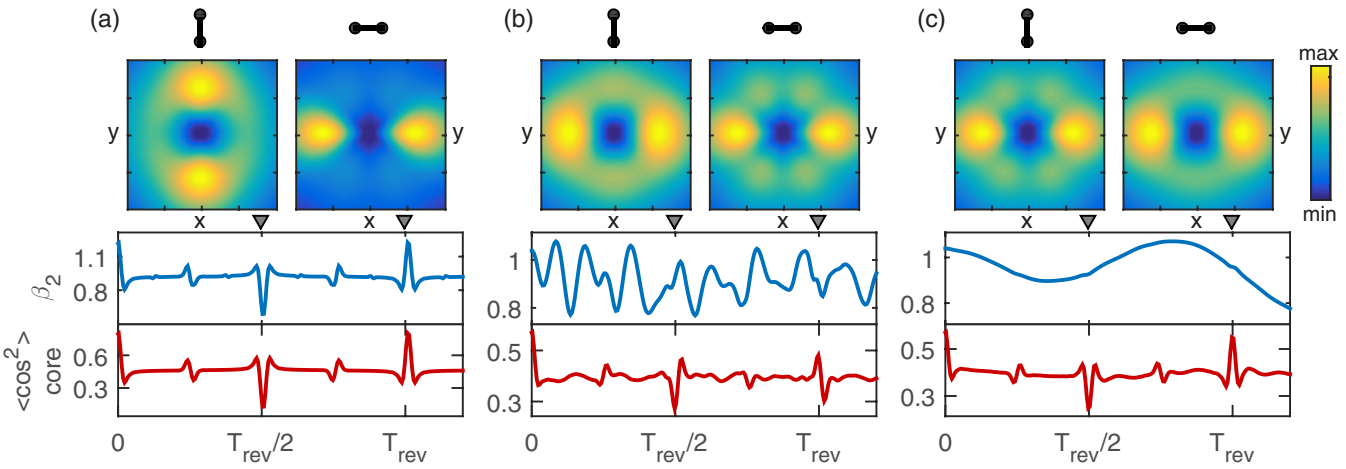

FIG. 2. The simulated electron and ion-core angular distribution time evolution of a nf Rydberg electron. A model N_2-like diatomic molecule is pumped to an nf Rydberg state with a five-photon excitation and subsequently probed through single-photon ionization (linear polarization of pump and probe along the x axis). The upper row of images show the electron position density of the Rydberg electron (before probing) at times corresponding to peak ion-core alignment and antialignment which occur near T_{rev} and $T_{rev}/2$. A $4f$ hydrogenic radial wave function is used for visualization. The molecular alignment direction for each image is depicted by the ball-and-stick graphic. The β_2 parameter of the photoelectron angular distribution and the $\langle\cos^2\rangle$ alignment value of the ion-core distribution is also shown. (a) Simulation for multiphoton excitation restricted to the $\Lambda = 0$ eigenstate of the f manifold with $a = 2400B$, where B is the rotational constant of the cation core. The PAD displays a typical Born-Oppenheimer molecular alignment signal. (b) and (c) Simulation for multiphoton excitation assuming all levels of the f manifold are accessible, with an electronic splitting of $a = 6B$ and $a = 0.6B$, showing the progressive development of l-uncoupled dynamics.

Figure 2 shows the simulated PAD for several values of the splitting parameter a. For excitation to an isolated substate of a manifold with large electronic splittings, the time-dependent PAD exhibits a typical Born-Oppenheimer molecular-frame alignment dependence [Fig. 2(a)]. As the electronic splitting decreases and all the manifold states are coherently populated [Fig. 2(b)], the l-uncoupling regime is approached and the PAD alignment signal no longer follows the *instantaneous* ion-core alignment, and rotational-electronic coupling significantly perturbs the dynamics of the ion-core rotational wave packet. For very small electronic splittings [Fig. 2(c)], a clear separation of the rotational and electronic time scales is achieved in what is sometimes referred to as a reverse Born-Oppenheimer regime.

We directly observe this dynamic l-uncoupling behavior in the $4f$ Rydberg manifold of N_2. We employ a $\approx$100 fs, 400 nm excitation pulse with a peak intensity of $\approx 10^{14}$W/cm^2. The pulse excites molecules to the $4f$ Rydberg manifold via a transient five-photon resonance due to the intensity-dependent ac Stark shift [27]. The electron wave packet is subsequently probed through single-photon ionization by a time-delayed, copropagating 800 nm pulse of similar duration and intensity as the pump pulse. The resulting photoelectron momentum distribution is collected using a velocity map imaging (VMI) spectrometer [28]. The pulses have linear polarizations parallel to each other and to the face of the microchannel plate. More information on the experimental setup can be found elsewhere [29].

The photoelectron angular distribution of the $4f$ Rydberg state is extracted from the momentum distribution by first subtracting the background pump-only ionization signal and then integrating over the energy width of the photoelectron peak.

The experimentally measured β_n values of the photoelectron distribution for room temperature N_2 as a function of pump-probe delay are shown in Fig. 3(b). The magnitude of β_n for $n > 8$ is negligible, as can be seen for β_{10}. This agrees with the identification of the Rydberg state as an f orbital since single-photon ionization selection rules dictate a maximum partial wave of $l = 4$, and hence a maximum nonzero β order of β_8 for an f orbital. Clear oscillatory signatures are seen in the β parameters, some of which survive longer than the full 30 ps scan range. The form and magnitude of these angular oscillations are shown in the polar plots in Fig. 3(a).

Although the initial multiphoton excitation must also coherently populate nuclear rotational states in N_2^+, the time-dependent PAD shows no direct correlation with the expected ion-core alignment dynamics of N_2^+. The simulated ion-core alignment for the multiphoton excited $4f$ state is shown in Fig. 3(c) along with the typical Born-Oppenheimer signal for comparison. The measured time-dependent PAD shows no evidence of the half and full rotational revival periods near 4.3 and 8.7 ps, which are the expected signatures of coherent rotational wave packets in Born-Oppenheimer molecular systems [3,30]. Instead, the quantum beats in the angular distribution correspond to the small electronic splittings of the $4f$ manifold in the presence of the anisotropic core. In the completely uncoupled regime described by Hund's case (d), selection rules dictate that the state of the core is unchanged during photoionization and hence different ion-core rotational states are not coupled together in the photoionization process [31]. The result is a PAD which is entirely insensitive to the molecular-frame motion. This is in contrast to the excitation of a low-lying valence electronic state, where the electron wave function follows the instantaneous orientation of the molecular frame and the time-dependent PAD exhibits large variation

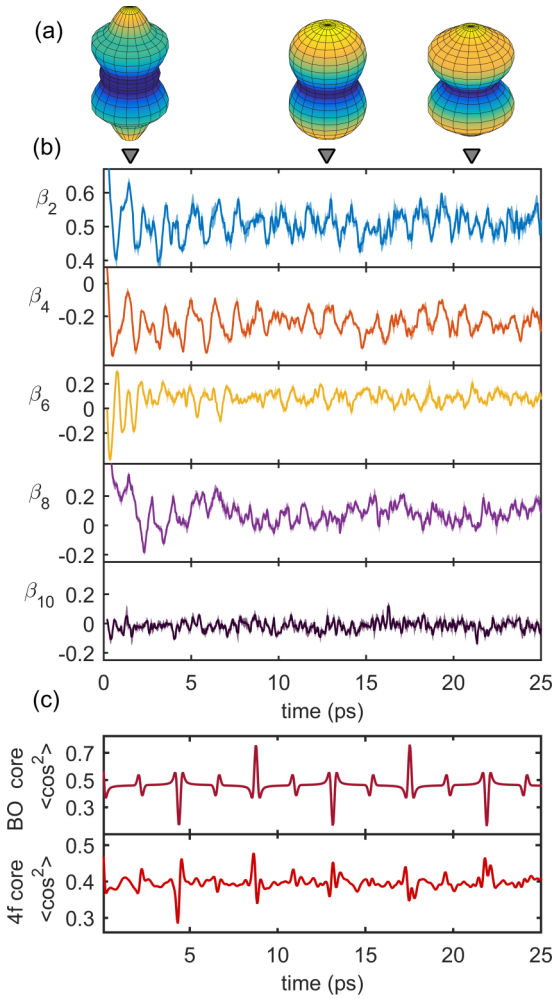

FIG. 3. Direct observation of l-uncoupling dynamics. (a) Polar plots of the experimentally extracted photoelectron angular distribution from the $4f$ Rydberg manifold in N_2 at selected probe times. (b) β values extracted from a least-squares fit of the data to Eq. (3). The error is plotted as a shaded region (where larger than the line thickness) corresponding to the standard error from three separate pump-probe scans. (c) Simulated ion-core alignment after multiphoton excitation in N_2. The top plot corresponds to excitation to a single Σ state in the Born-Oppenheimer regime, while the lower plot shows the expected ion-core alignment signal for excitation to the $4f$ Rydberg manifold.

in the β parameters only near the quantum revivals of the rotational wave packet [3,30].

The observed time-dependent PAD of the $4f$ manifold can be compared to the model l-uncoupling simulation. Our model employs spectroscopic values for the $4f$ electronic energies in the vibrational ground state of N_2 [14], rather than the approximate form given by Eq. (2). The amplitude and phase of the discrete Fourier transform of the time-dependent β_2

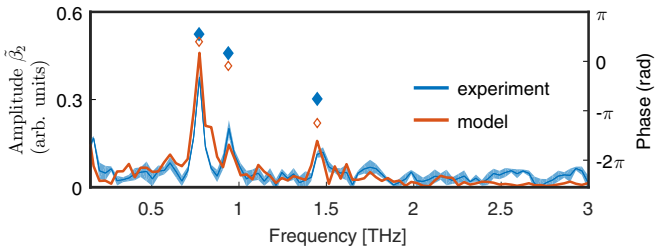

FIG. 4. Fourier analysis. The amplitude of the discrete Fourier transform of the time-dependent β_2 value is shown for both experiment and model. The shaded area around the experimental curve corresponds to the standard error from the three separate pump-probe scans. The phases of the three prominent frequency components are also plotted for experiment and model (diamond markers). The standard errors of the extracted phases are smaller than the marker dimensions.

values from both experiment and model are shown in Fig. 4. The model reproduces the main quantum beat frequencies seen in the experiment, which occur in the 0.7–1.5 THz (700 fs–1.4 ps) range. The extracted phases of the prominent frequency components are also plotted. The modeled phase values agree quite well with the measured phases, suggesting that the impulsive five-photon excitation model provides an adequate description of the pump process. The discrepancy in phases amount to shifts of <170 fs, close to the duration of the excitation pulse and the limits of the impulsive model. Simulations of the higher order β parameters show lower frequency oscillations (<0.5 THz) that are not present in the experimental signal. This discrepancy may be due to coupling to nearby perturbing electronic states in N_2 [14,15], angular distortion inherent to noninverted VMI images, or from the nonperturbative nature of the pump pulse [32].

In summary, we have used time-resolved photoelectron angular distributions to image the dynamics of the non-Born-Oppenheimer l-uncoupling regime in the laboratory frame. The complex behavior of the electron motion in this regime is radically different from low-lying valence state molecular-frame motion. Future studies in which the ion-core and photoelectron angular distributions are simultaneously measured would be highly beneficial in allowing for a direct experimental comparison of the rotational and electronic motion of the l-uncoupled system. In addition, the coherent excitation of l-uncoupled electronic states shown in this work, when combined with existing rotational wave-packet preparation techniques [25,33], offers the prospect of creating unique and exotic electronic-rotational wave packets not possible in Born-Oppenheimer systems.

This work was supported by the AMOS program, Chemical Sciences, Geosciences, and Biosciences Division, Basic Energy Sciences, Office of Science, U.S. Department of Energy.

[1] C. Z. Bisgaard, O. J. Clarkin, G. Wu, A. M. D. Lee, O. Geßner, C. C. Hayden, and A. Stolow, Science **323**, 1464 (2009).

[2] P. Hockett, C. Z. Bisgaard, O. J. Clarkin, and A. Stolow, Nat. Phys. **7**, 612 (2011).

[3] C. Qin, Y. Liu, S. Zhang, Y. Wang, Y. Tang, and B. Zhang, Phys. Rev. A **83**, 033423 (2011).
[4] O. Geßner, A. M. D. Lee, J. P. Shaffer, H. Reisler, S. V. Levchenko, A. I. Krylov, J. G. Underwood, H. Shi, A. L. L. East, D. M. Wardlaw, E. t. H. Chrysostom, C. C. Hayden, and A. Stolow, Science **311**, 219 (2006).
[5] F. Kelkensberg, A. Rouzée, W. Siu, G. Gademann, P. Johnsson, M. Lucchini, R. R. Lucchese, and M. J. J. Vrakking, Phys. Rev. A **84**, 051404(R) (2011).
[6] J. B. Williams, C. S. Trevisan, M. S. Schöffler, T. Jahnke, I. Bocharova, H. Kim, B. Ulrich, R. Wallauer, F. Sturm, T. N. Rescigno, A. Belkacem, R. Dörner, T. Weber, C. W. McCurdy, and A. L. Landers, Phys. Rev. Lett. **108**, 233002 (2012).
[7] I. V. Litvinyuk, K. F. Lee, P. W. Dooley, D. M. Rayner, D. M. Villeneuve, and P. B. Corkum, Phys. Rev. Lett. **90**, 233003 (2003).
[8] M. Meckel, A. Staudte, S. Patchkovskii, D. M. Villeneuve, P. B. Corkum, R. Dörner, and M. Spanner, Nat. Phys. **10**, 594 (2014).
[9] A. Staudte, S. Patchkovskii, D. Pavičić, H. Akagi, O. Smirnova, D. Zeidler, M. Meckel, D. M. Villeneuve, R. Dörner, M. Y. Ivanov, and P. B. Corkum, Phys. Rev. Lett. **102**, 033004 (2009).
[10] L. Holmegaard, J. L. Hansen, L. Kalhøj, S. Louise Kragh, H. Stapelfeldt, F. Filsinger, J. Küpper, G. Meijer, D. Dimitrovski, M. Abu-samha, C. P. J. Martiny, and L. Bojer Madsen, Nat. Phys. **6**, 428 (2010).
[11] R. S. Mulliken, J. Am. Chem. Soc. **86**, 3183 (1964).
[12] G. Herzberg and Ch. Jungen, J. Chem. Phys. **77**, 5876 (1982).
[13] R.-Y. Chang, C.-C. Tsai, T.-J. Whang, and C.-P. Cheng, J. Chem. Phys. **123**, 224303 (2005).
[14] K. P. Huber, Ch. Jungen, K. Yoshino, K. Ito, and G. Stark, J. Chem. Phys. **100**, 7957 (1994).
[15] Ch. Jungen, K. P. Huber, M. Jungen, and G. Stark, J. Chem. Phys. **118**, 4517 (2003).
[16] Ch. Jungen and E. Miescher, Can. J. Phys. **47**, 1769 (1969).
[17] E. F. McCormack, S. T. Pratt, J. L. Dehmer, and P. M. Dehmer, Phys. Rev. A **44**, 3007 (1991).
[18] P. Labastie, M. C. Bordas, B. Tribollet, and M. Broyer, Phys. Rev. Lett. **52**, 1681 (1984).
[19] R. A. L. Smith, V. G. Stavros, J. R. R. Verlet, H. H. Fielding, D. Townsend, and T. P. Softley, J. Chem. Phys. **119**, 3085 (2003).
[20] W. Li, T. Pohl, J. M. Rost, S. T. Rittenhouse, H. R. Sadeghpour, J. Nipper, B. Butscher, J. B. Balewski, V. Bendkowsky, R. Löw, and T. Pfau, Science **334**, 1110 (2011).
[21] H. H. Fielding, Annu. Rev. Phys. Chem. **56**, 91 (2005).
[22] J. Hougen, *National Bureau of Standards Monograph 115* (U.S. Government Printing Office, Washington, DC, 1970).
[23] J. M. Brown and A. Carrington, in *Rotational Spectroscopy of Diatomic Molecules*, Cambridge Molecular Science (Cambridge University Press, Cambridge, UK, 2003).
[24] E. E. Eyler, Phys. Rev. A **34**, 2881 (1986).
[25] A. Korobenko and V. Milner, Phys. Rev. Lett. **116**, 183001 (2016).
[26] See Supplemental Material at http://link.aps.org/supplemental/10.1103/PhysRevA.95.061403 for additional details on the experiment and analysis, as well as a movie of the molecular uncoupling simulation in Fig. 1.
[27] K. L. Knappenberger, Jr., E.-B. W. Lerch, P. Wen, and S. R. Leone, J. Chem. Phys. **127**, 124318 (2007).
[28] A. T. J. B. Eppink and D. H. Parker, Rev. Sci. Instrum. **68**, 3477 (1997).
[29] L. J. Zipp, A. Natan, and P. H. Bucksbaum, Optica **1**, 361 (2014).
[30] M. Tsubouchi, B. J. Whitaker, L. Wang, H. Kohguchi, and T. Suzuki, Phys. Rev. Lett. **86**, 4500 (2001).
[31] J. Xie and R. N. Zare, J. Chem. Phys. **93**, 3033 (1990).
[32] S. C. Althorpe and T. Seideman, J. Chem. Phys. **110**, 147 (1999).
[33] H. Stapelfeldt and T. Seideman, Rev. Mod. Phys. **75**, 543 (2003).

Imaging the breakdown of molecular-frame dynamics through rotational uncoupling - Supplemental Material

Optical pulse preparation. A ≈100 fs 800 nm pulse from a Ti:Sapphire laser was frequency doubled in a BBO crystal cut for Type I second harmonic generation. The residual 800 nm pulse and the 400 nm pulse were then split and recombined in a Mach-Zehnder interferometer using dichroic beam splitters. The delay between the two pulses was controlled by varying the path length of one arm with a motorized translation stage. The intensity of the pulses were set by a separate wave plate in each arm. After recombining, the two pulses co-propagate and pass through a wire grid polarizer before entering a vacuum chamber backfilled with room temperature N_2 gas at a pressure of several 10^{-8} millibar. The pulses are then focused by a spherical mirror with a 15 cm focal length into a velocity map imaging (VMI) spectrometer.

Extracting the $4f$ photoelectron angular distribution. The pump-probe delay was varied between -1 to 30 ps with 700 equally spaced delay points corresponding to $\sim$ 45 fs increments, and the photoelectron momentum distribution was collected at each delay. An example of the raw VMI photoelectron distribution is shown in Fig. S1. The delay points were visited in a randomized order to mitigate any effects caused by long-term drifts of the laser system. The collected photoelectron distribution includes electrons ionized by the 800 nm probe pulse as well as the intense 400 nm pump pulse. In order to eliminate the ionization signal generated by the pump, a background momentum distribution is collected with the 800 nm beam blocked. This distribution is then normalized and subtracted from each pump-probe electron momentum distribution. A moving average of three adjacent delay points is then implemented in order to improve the angular distribution signal.

The photoelectron peak corresponding to the $4f$ Rydberg manifold is then integrated over in the radial momentum direction. In order to set the limits of integration, we first perform an inverse Abel transform of the raw photoelectron distribution using a polar onion peeling algorithm [1] to get the undistorted angle-integrated momentum distribution, shown in Fig. S2(a). The upper and lower limits of integration are then chosen at the 20% level of the maximum amplitude of the 4f photoelectron peak in the angle-integrated, Abel-inverted momentum distribution. Taking these limits, we then integrate over this region in the raw momentum distribution as depicted in Fig. S2(b). By restricting

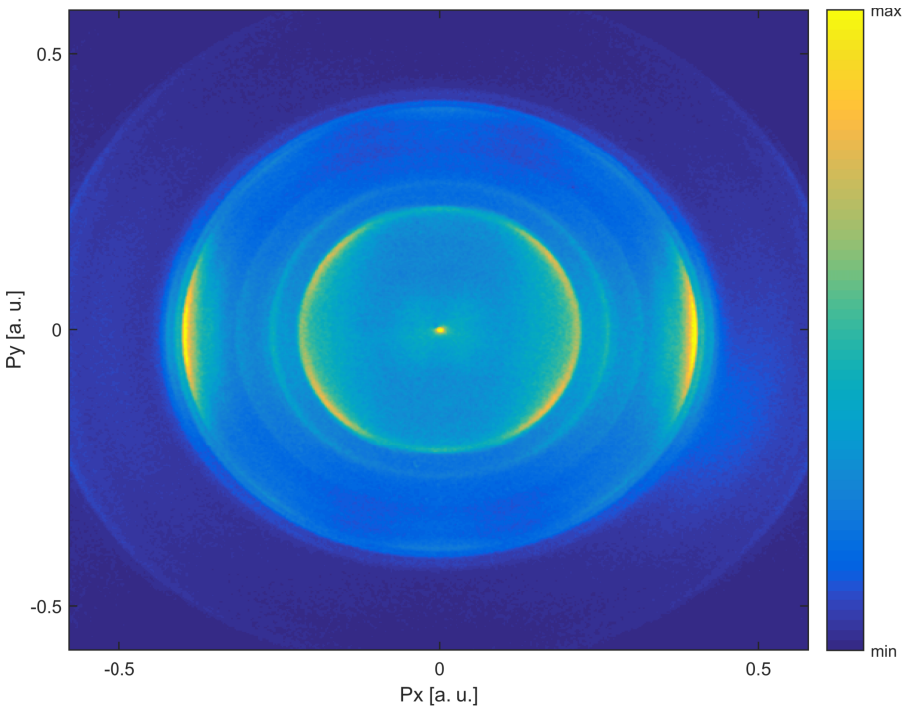

FIG. S1. Raw VMI photoelectron momentum distribution. The innermost bright ring corresponds to single photon ionization of the $4f$ Rydberg state.

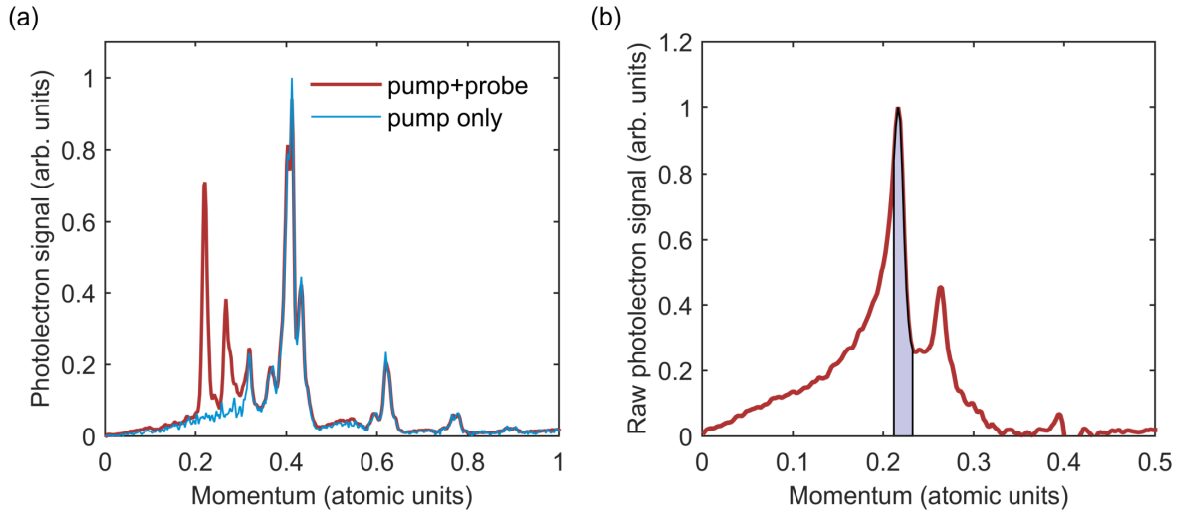

FIG. S2. (a) The Abel-inverted photoelectron momentum distribution from N_2 comparing the pump only signal with the pump+probe signal. The lowest energy photoelectron peak of the pump+probe signal corresponds to the $4f$ manifold. (b) The raw photoelectron momentum distribution showing the region of the spectrum (shaded area) that is included in the angular distribution extraction of the $4f$ photoelectron signal.

the integration to this region we limit distortions of the angular distribution due to the "pancaking" of the momentum distribution perpendicular to the detector in a velocity map imaging spectrometer. We then utilize the four-fold symmetry of the system, summing the four angular quadrants together before fitting the angular distribution to a sum of even-ordered Legendre polynomials (Eq. (3) in the main text) using a least-squares method.

Fourier transform of the time-dependent PAD The discrete Fourier transforms of the measured and modeled β_2 parameter is taken after applying a periodic Hamming window. The signal used in the Fourier transform spans from 300 fs to 30 ps, in order to eliminate transient nonlinear effects when the pump and probe pulses are overlapped in time.

Energy levels of the $4f$ manifold in N_2

In Fig. S3, the energies of the $4f$ manifold states as a function of rotational number are plotted with the spectator ion-core rotational energy $BR(R+1)$ subtracted from the total. The energies are computed from the Hamiltonian

$$H = \hat{H}_{ev} + B\hat{R}^2, \tag{1}$$

where $\hat{H}_{ev} = -\frac{1}{2(n-\mu_\Lambda)^2}$ is measured relative to the vibrational ground state ionization potential, n is the principal quantum number, and the quantum defect values δ_Λ are taken from Ref. [2]. The energies of the Rydberg manifold states, denoted by their Hund's case (d) quantum label $\mathcal{L} = J - R$, approach asymptotic values in the limit of large rotations. The quantum label $\mathcal{L}$ can be interpreted as the projection of the electron orbital angular momentum onto the *rotational* axis [3].

***l*-uncoupling Hamiltonian matrix elements.** The rotational-electronic Hamiltonian in Eq. (1) of the main text may be written in terms of angular momentum operators referred to the molecular frame [4]:

$$\begin{aligned}\hat{H} &= \hat{H}_{ev} + B\hat{R}^2 = \hat{H}_{ev} + B[(\hat{J}_x - \hat{l}_x)^2 + (\hat{J}_y - \hat{l}_y)^2] \\ &= \hat{H}_{ev} + B[(\hat{J} - \hat{J}_z)^2 + (\hat{l} - \hat{l}_z)^2 - (\hat{J}_+\hat{l}_- + \hat{J}_-\hat{l}_+)],\end{aligned} \tag{2}$$

where $\hat{J}$ is the total angular momentum $\hat{l}$ is the Rydberg electron orbital angular momentum, $\hat{J}_\pm$,$\hat{l}_\pm$ are raising and lowering operators, and the coordinates are referred to the molecular frame with the internuclear axis along the z-axis. We ignore electron spin in this treatment, since we are concerned with singlet states of N_2.

The matrix elements of the Hamiltonian are then easily calculated in a Hund's case (b) basis if an integer value of the electron orbital angular momentum is assumed, which is a very good approximation for non-penetrating, high l molecular Rydberg states. The matrix elements of the angular momentum operators referred to the molecular frame are calculated analogously to lab frame operators, with the exception of the $\hat{J}_\pm$ operators, which exhibit an anomalous sign [4]:

$$\langle J, (\Lambda+1)|J_\pm|J, \Lambda\rangle = \sqrt{(J \pm \Lambda)(J \mp \Lambda + 1)}. \tag{3}$$

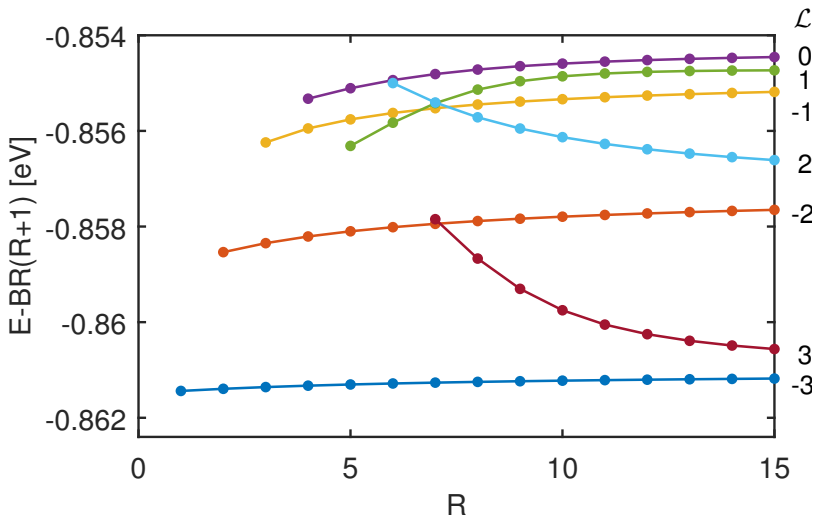

FIG. S3. Energies of the $4f$ Rydberg manifold in N_2. The energies of the substates are plotted as a function of the core rotational number R, with the spectator rotational energy subtracted. The states are labeled according to the Hund's case (d) value of $\mathcal{L} = J - R$.

We obtain an energy submatrix for each value of J, which we then diagonalize to calculate the field-free dynamics of the l-uncoupling.

Retrieving the simulated lab frame angular distributions. After field-free propagation of the l-uncoupled wave packet, the molecular wave function is projected from Hund's case (b) basis states $|J, M, l, \Lambda\rangle$, onto the completely uncoupled Hund's case (d) states $|J, M, l, R\rangle$. This is achieved using the vector coupling relations of the molecular frame referenced angular momenta, taking care of the proper phase conventions [5]:

$$|J, M, l, R\rangle = \sum_{\Lambda} (-1)^{R-J-\Lambda} \langle J, \Lambda; l, -\Lambda | R0\rangle |J, M, l, \Lambda\rangle, \tag{4}$$

where the prefactor in brackets is a Clebsch-Gordan coefficient. From the case (d) basis, the lab frame decoupled electron and ion-core wave functions may then be obtained by a straightforward application of angular momentum coupling:

$$|l, m_l\rangle |R, m_R\rangle = \sum_{J,M} \langle JM | l, m_l; R, m_R\rangle |J, M, l, R\rangle. \tag{5}$$

Quasi-classical l-uncoupling demonstration. For the visualization in Fig. 1 of the main text, an initial rotational state is prepared as a superposition of $|J, M\rangle$ states where J is even valued and $J = M$ for all states. The Gaussian-weighted distribution is centered at $|J = 30, M = 30\rangle$ with a full width at half maximum of $\Delta J = 5$. This localized rotational wave packet approaches the form of a quasi-classical rotating rigid rotor.

Simulating the multiphoton excitation and photoionization. Dipole matrix elements are calculated in the single active electron approximation, modeling the N_2 ground state σ_g orbital as an equal superposition of s and d partial waves. The rotational $|JM\rangle$ states are initially populated with a thermal distribution corresponding to a temperature of 295 K for N_2. We include up to a maximum rotational state of $J = 20$. The angular factors of the dipole matrix elements are then calculated exactly, rigorously preserving all selection rules. The direction cosine matrix elements are evaluated with the use of tabulated values [4]. The radial factors are approximated with a propensity term that favors $l \to l + 1$ over $l \to l - 1$ transitions by a factor of 2. The final photoionization step is calculated after projection of the molecular wave function onto the decoupled $|l, m_l\rangle |R, m_R\rangle$ basis. In evaluating the dipole matrix elements between the $4f$ and continuum states, we use hydrogenic radial wave functions, which provide a good approximation for these high l states due to their small quantum defects.

[1] G. M. Roberts, J. L. Nixon, J. Lecointre, E. Wrede, and J. R. R. Verlet, Review of Scientific Instruments **80**, 053104 (2009).

[2] K. P. Huber, C. Jungen, K. Yoshino, K. Ito, and G. Stark, The Journal of Chemical Physics **100**, 7957 (1994).
[3] H. Lefebvre-Brion and R. W. Field, in *The Spectra and Dynamics of Diatomic Molecules* (Academic Press, San Diego, 2004) pp. 87–231.
[4] J. Hougen, *National Bureau of Standards Monograph 115* (U.S. Government Printing Office, 1970).
[5] J. M. Brown and B. J. Howard, Molecular Physics **31**, 1517 (1976).